Rooftop analysis for solar flat plate collector assessment to achieving sustainability energy

Perea-Moreno, Alberto-Jesús[1], García-Cruz, Amós [2], Novas, Nuria[2], Manzano-Agugliaro, Francisco [2, *]

[1] Dpt. of Applied Physics. CEIA3. University of Cordoba. Campus de Rabanales. 14071 Cordoba. Spain

[2] Dpt. of Engineering and CIAIMBITAL (Research Center on Agricultural and Food Biotechnology). CEIA3. University of Almeria, Almeria, 04120, Spain

* Author to whom correspondence should be addressed: fmanzano@ual.es

Abstract

The insufficiency of current energy sources, elevated costs and global climate worriment are distinctive factors making of renewable energy an issue of boosting consideration. In this concern, solar energy is viewed as being indefinitely environmental friendly, carbon-free, beneficial nature with appreciated cost potentials and is witnessing fast progressing. Following the Horizon 2020 climate and energy package, the volume of gases emitted by greenhouses has to be cut down by 20% by all the European Union (EU) member countries in order to enhance energy performance by 20% and raise the renewable energy rate to 20% by 2020. Solar energy on building roofs plays a crucial aspect in renewable and sustainable energy consumption of high-density human habitats. A merest energy should be allocated to provide hot water service from solar sources, as other European norms for new buildings by the Spanish Technical Building Code, similarly to other European regulation on achievement objectives. The climate zone and the overall demand of hot water in the building regulate this minimal amount needed. This manuscript use a new methodology for automatic detection of geometric patterns from aerial or space images using a Hierarchical Temporal Memory (HTM) algorithm. In this way, an automatic method for the identification of building roofs in order to assess the opportunities available to install solar thermal systems in small urban areas has been developed. As case of study: a village with 7,000 inhabitants was analyzed in the South of Spain. The maximum overall accuracy obtained among the different classifications made was 98.05%, avoiding problems related to the use of images with high spatial resolution, as in the salt-and-pepper noise effect. This approach contributes reducing the generated carbon and GHG emissions and open new perspectives for energy savings strategies to optimize the energy efficiency of buildings. In the case study, implementing the solar thermal systems would come out with a saving of 1.4 tons of CO_2 per inhabitant.

Keywords: sustainability; solar thermal system; solar energy; energy saving; pattern recognition; building roof

 Published as:Alberto-Jesús Perea-Moreno, Amós García-Cruz, Nuria Novas, Francisco Manzano-Agugliaro,Rooftop analysis for solar flat plate collector assessment to achieving sustainability energy, Journal of Cleaner Production, Volume 148, 2017, Pages 545-554, ISSN 0959-6526, https://doi.org/10.1016/

Table of Acronyms

Acronym	Concept
API	Application Programming Interface
$belief_i$	Probability of similarity
D	Dimension of the vector
DSM	Digital Surface Model
ED50	European Datum 1950
HTM	Hierarchical Temporal Memory
It	Increment
LiDAR	Light Detection and Ranging
maxDist	maxDistance
OBIA	Object-based Image Analysis
outputElementCount	Categories
PV	Solar Photovoltaic
requestGroupCount	Temporal groups
ScaleCount	Scale factor
scaleRF	Scale reference
SD	*Standard Deviation*
spatialOverlap	Spatial overlap
spatialRF	Spatial reference
UAV	Unmanned Aerial Vehicle

1. Introduction

In the last decades, the raise in energy interest made energy employment a crucial affair on large scale implementation (Baños et al. 2011). In the same concern, various environmental complications have arisen from the use of fossil fuels and other conventional energy sources (Perea-Moreno et al., 2016). Alternative energy sources are the best focus solution to be explored due to the problems resulting from destructive substances released into the atmosphere resulting in climate change and global warming (Almeida et al., 2017). An explicit consequence of the EU strategy "20-20-20", the sustainability of urban areas promises to produce energy from renewable sources and to announce an extensive legislation on energy efficacy (Cadez and Czerny, 2016).

An assessment of the renewable energy potentials is required to define clear regional energy arrangements (e.g. national). In the recent years, a significant aspiration has been achieved towards this appreciation in various worldwide regions (Castellano et al., 2015).

A considerable amount of energy is consumed by the building sector and major profits can be granted to approach zero or nearly zero energy building by handling renewable energy technologies (Manzano-Agugliaro et al., 2015). Whether ensured through solar thermals systems or solar photovoltaic (PV), solar energy is considered as an abundant, free and clean alternative energy source (Fernández-García et al. 2015).

Sustainability is based on three pillars: economic, social and environmental, with an occasionally fragile and difficult balance among the pillars (Almeida et al., 2017). Due to the enormous number of entities to take into consideration (e.g, millions of buildings in a country), estimating the energy engendered by solar thermal systems in building is seen as the most complicated among the applicable technologies (AlFaris et al., 2016). Although complex, such information is treasured for the enlargement of efficient building energy codes. Similarly, to other European norms established on achievement objectives, the Code of Technical Building in Spain (MVIV, 2009) stands for assuring a minimum amount of energy for hot water service from solar sources which bets on the climate zone and the overall water demand in the building. For the case of Spain, 70% is the recorded percentage from the overall hot water demand except for the ultimate challenged zones. For optimization purposes of the vacant area, the remaining roof area can be invested for PV systems, for example, in order to upgrade once this requirement is satisfied. Upon this, it is relatively essential to estimate the possible roof-top areas in urban areas.

Practically, estimation of the solar energy potential in urban setting can be applied differently from simple estimations to airborne LiDAR technologies (Szabó et al. 2016).

Automatic scanning of the buildings is possible with the latter methods, with building a 3D model of the city as well.

For example, a solar 3D urban model of the Campus of the University of Lisbon was developed to evaluate the solar resource of buildings and integrate the potential of roofs with that of facades. To assess this potential, a digital surface model (DSM) of the urban region was built from LiDAR data (Redweik et al., 2013).

Unless a convincing extent of manual work is done, the cited technologies do include some major error which becomes a disadvantage. Moreover, many decision makers do not accept to implement these technologies with practically elevated cost of software and equipments (Torres-Sánchez et al., 2015).

Based on building typology, a substitute approach to determine roof-top areas of urban areas in described in this paper.

For this purpose, information of important use can be analysed and extracted from the images through the employment of powerful and automatic software. In order the Object-based Image Analysis (OBIA) techniques are applied not only for a high level of adaptability but automation as well. These techniques overcome some constraints of pixel-based methodology by combining neighbouring pixels with a homogeneous spectral value after a partition process to use the conceived objects as the primary elements for analysis (Martínez-Rubio et al., 2016). Subsequently, OBIA merge spectral, topographic and contextual information for those items to perform more complex classifications. These techniques have been successfully applied to images obtained by UAVs in urban areas (Kohli et al., 2016).

In recent years, the technology involved in remote sensing and object recognition has considerably advanced (Andreopoulos and Tsotsos, 2016; Li et al., 2015a), with diverse applications ranging from recognition and vehicle classification (Battiato et al., 2015) to the facial recognition of individuals (Siddiqi et al., 2015). Studies on detection and object recognition can be classified into two categories: keypoint-based object detection (Hare et al. 2012) and hierarchical and cascaded classifications (Li et al., 2013). Parallel to this development, a new technology applicable to the classification of digital pictures emerged: the Hierarchical Temporal Memory (HTM) learning algorithm. This classification technology is based on both neural networks and Bayesian networks but involves a particular algorithm based on a revolutionary model of human intelligence – the memory-prediction theory developed by Jeff Hawkins (Hawkins and Blakeslee, 2004). This assumption relies on the workings of the human cerebral cortex, which has architecture in the form of "layers" in which information flows bidirectionally from the senses to the brain. From this operating hierarchy, a hypothesis of how the human mind works is created. The key point of this algorithm is found in the duality of the information received. All information we perceive has a spatial component and a temporal one; information is received by the human brain not as an isolated pattern but as a succession of patterns. The cerebral cortex stores the patterns that we perceive and how they are ordered in time. In light of that concept, the memory-prediction theory states that the cerebral cortex stores the new patterns and their evolution over time so that once these sequences stabilize the brain can make predictions (or inferences) enabling it, without

observing a full sequence, to know what pattern it is observing because it knows the sequence in which the patterns occur over time (Hawkins and Blakeslee, 2004).

Thus, this new technology developed by Jeff Hawkins not only presents a new model of how human intelligence functions but also models a neural network system capable of emulating this theory. This classification technology is not specific to image analysis but is versatile for any type of information (from medical information to economic data), with a dual role: learning and pattern recognition in data flows and classifying unknown data according to the training received. Currently, we can find this technology integrated into the free software application NuPIC developed by NUMENTA®, which is used to classify data streams (Hawkins et al., 2011). These data can be of many types, ranging from sign language (Rozado et al., 2012) to eye retinal images for biomedical purposes (Boone et al., 2010). There are open areas of research using HTM as a classifier for land planning, which is where our work focuses. In a previous study, Perea et al. (2009) conducted an analysis of high-resolution images for classification and land planning in agricultural environments; starting from images from a UltracamD® photo sensor of a region of southern Spain, classification results were obtained that recognized the ground cover up to 90.4 %.

Thus, given the positive results previously obtained in the classification of images, the aim of this paper is to propose a new methodology for automatic detection of geometric patterns (solar flat collector) in rooftops from aerial or space images in order to appraise the opportunities feasible to feat solar thermal systems in small urban areas.

2. Material and Methods

2.1. Study site

The area of study comprises the city of Hinojosa del Duque (38º33’ and 38º23’ N; 5º16’ and 5º50’ W); it was located at Pedroches Valley at Cordoba Province in Spain (Figure 1).

On 23 May 2006, the sensor of Vexcel UltracamD photogrammetric captures 64 frames with dimensions of 7 500 x 11 500 pixels with 8 bits encoding to carry out the study. Consisting of infrared, green and blue bands, the frames had a spatial resolution around 0.5m. Orthorectification was applied to these frames that make reference to ED50 (European Datum 1950).

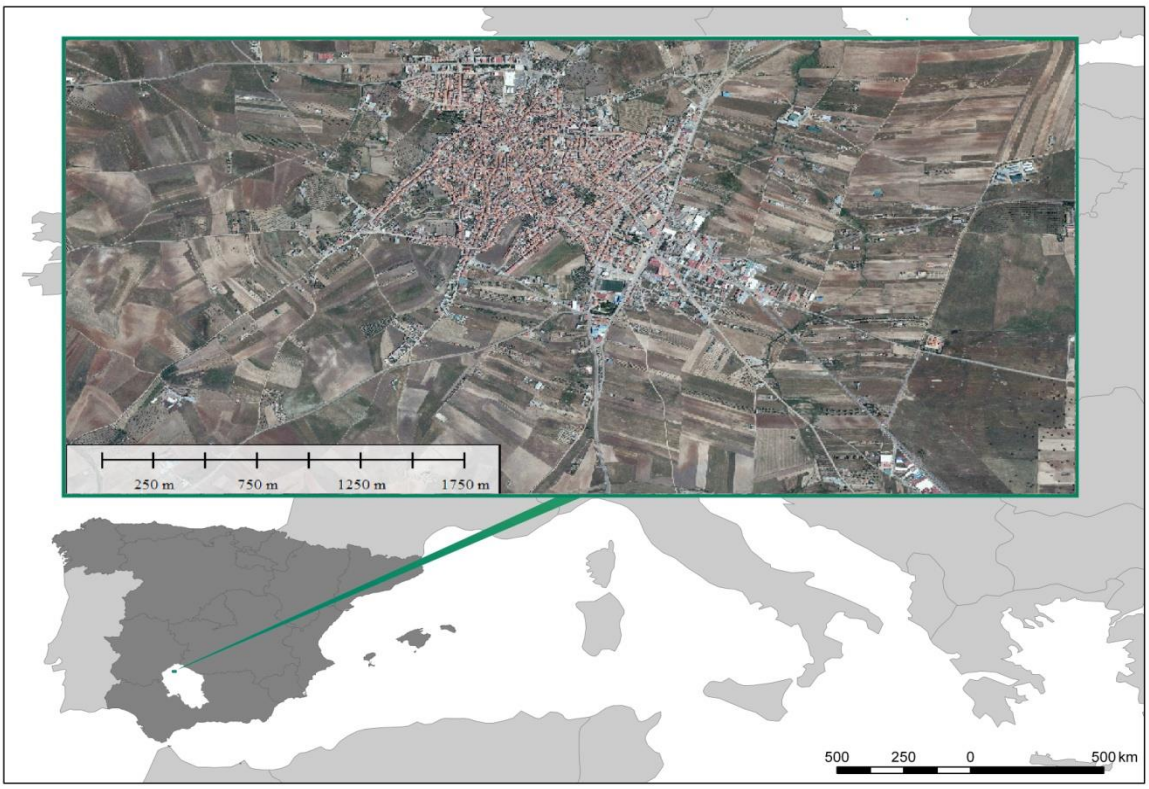

Figure 1. Location map.

2.2. Sensor Description

On 15 April 2015, an Ultracamd® sensor of Vexcel has given the 7500 x 11500 pixels photogram that has been used as dataset for this research. Basically, red, green and blue form the band combination of this photogram and a 30 cm resolution is assigned to the digital aerial photographs.

In order for the classifications to be validated, the training areas to be selected, the image to be orthorectified, digital terrain models were used next to digital vector maps and color orthophotos. Land uses were determined after a visit for the study area and the UTM system (ED-1950, UTM-Zone 30N) was used to project the data map.

The development of this system resides in distinguishing between building roof with solar thermal system and building roof without solar thermal system (Figure 2).

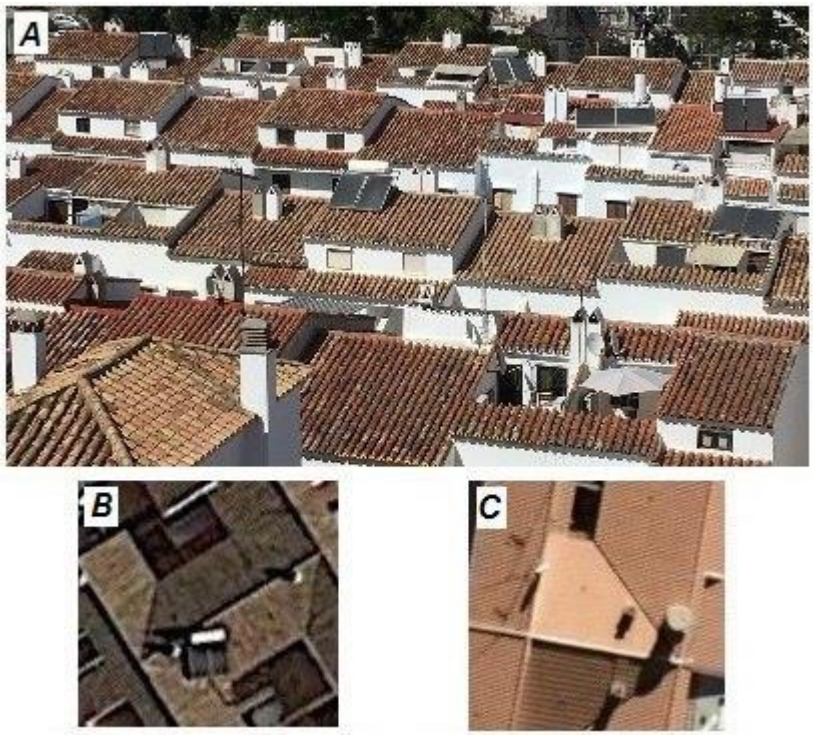

Figure 2. Land covers used in this study: A) Global view, B) With Solar Thermal, C) Without Solar Thermal

2.3. HTM methodology

A space and time hierarchical structure defines all the objects in the world. This same concept is used by HTM to generate a series of interconnected nodes organized in a tree hierarchy (Numenta Inc., 2010). Thus, structure of the world is efficiently represented by a hierarchical HTM in space and time (Hawkins and George, 2007).

If we analyze the full name of the algorithm (Hierarchical Temporal Memory), we can distinguish that the columns are the smaller elements that make up a pyramid shaped hierarchy levels to form a HTM network referred as “Hierarchical”. This network can be trained on temporal sequences data so it is called “Temporal”. Moreover, it has the capability to accumulate huge set of spatial patterns and temporal sequences efficiently so it is “Memory”. All these make the HTM model capable of predicting and inferring the received patterns adequately (Numenta Inc., 2010).

The HTM learning algorithm implemented in the Nupic free Application Programming Interface (API) was used in this experiment. This API allows easy implementations of HTM learning algorithms using real world images. Although this software can be used in a mixture of contexts, in this paper we target only on visual recognition applications. Through Python scripts, building, configuration and writing of this API is made. Because the majority of the scripts have a distinct arrangement standardized for each of them, customization is required for each network. Designing and configuring the hierarchy of nodes

require from the researchers taking maximum advantage of their data. Each node encounters several input values based on which its algorithms will be customized. Seeking the improvement of accuracy, a double tweak of the node configuration values is needed due to the large amount of node parameters.

Figure 3 presents the overall methodology for HTM design and implementation. There are five phases in this methodology, from the definition and configuration of the data and HTM network to the training and its evaluation.

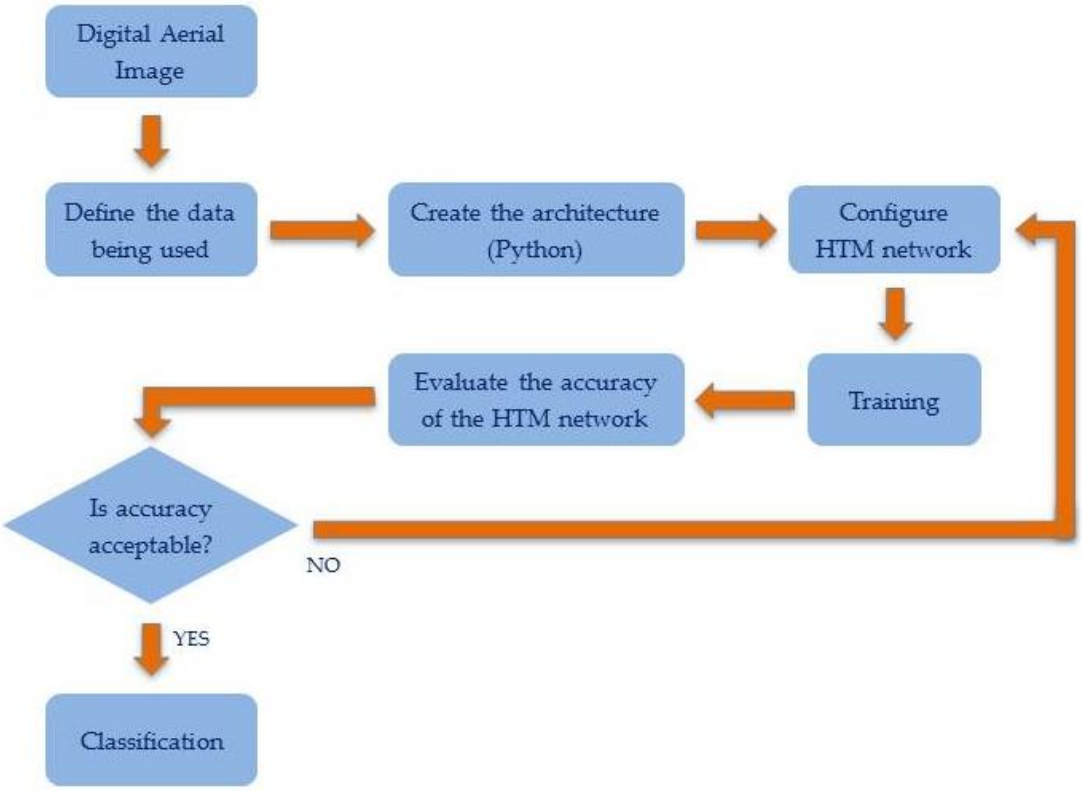

Figure 3. Overall methodology diagram.

Once the data to be used have been defined, two steps were necessary to create this network: the creation of the architecture using the Python programming language and the formation of a set of training patterns. Based on the experience of the research group in previous work (Perea et al., 2009, 2012a, 2012b), the HTM network was defined in three levels: the first two levels, having two sub-levels each (the level that analyses the spatial component and another level that analyses the temporal component), and a concluding classifier. This classifier is the ultimate element of the hierarchy and sorts the images into similar categories. The level 1 or input level is composed of 8x8 input nodes, each associated to a single pixel. Nodes from the first level go through the raw image and receive a characteristic of the training pattern image, creating an entry vector formed by digital levels of 8x8 pixels. Level 2 is composed of 16 nodes that receive the information from the previous level; therefore, each level 2 node has 4 primary child nodes (arranged in 2x2 region). And finally, level 3 or higher comprises a single node, and it has 16 child nodes (4x4 region) and a receptive field of 64 pixels. In Figure 4, the downward

connection of one node per level is shown. This system operates in two phases: the training phase and the inference phase. At the time of the training phase, the network is revealed to training patterns, and a model that classifies patterns into categories is built. Through the inference phase, new patterns are generated in these categories through the network distribution. All nodes (except the initial node) process information in the same manner and consist of two modules: temporal and spatial (George and Jaros, 2007). Understanding an HTM node involves understanding the operation of these modules during the learning and training phases.

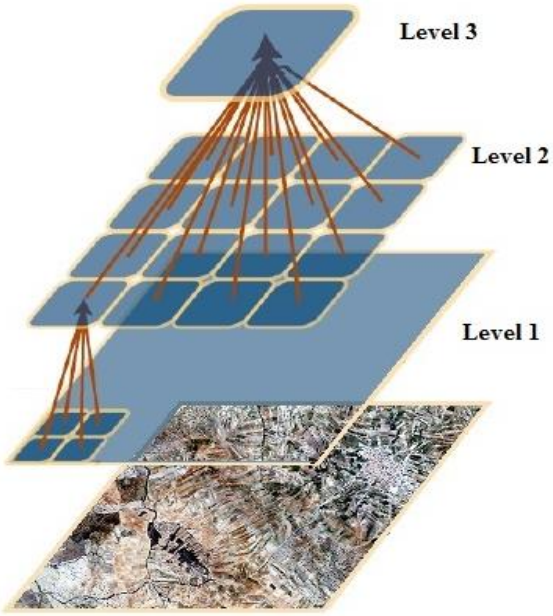

Figure 4. Details of the HTM structure. Level 1 is composed of 64 nodes; level 2 is composed of 16 nodes and level 3 comprises a single node.

2.3.1. Training phase

During the training phase, the spatial module learns to classify input data based on the spatial coincidence of the elements that compose them. The input vector is compared with other vectors already stored. The exit of the spatial module (temporal module entrance) occurs in terms of their matches and can be noticed as a pre-processing stage for the temporal module, clarifying entry. The temporal module receives temporary groups that exist regularly as groups of coincidence (George and Jaros, 2007).

2.3.1.1. Spatial module

Raw data is received by the spatial modules of the input nodes from the sensor; the output data is received by the spatial modules of the upper nodes from their lower nodes. The concentration of the order is the input of the spatial module in the upper layer set by the output of the nodes below. A series of vectors represent its input, where building a matrix (match matrix) of input vectors that have recently occurred is the function of the spatial module.

Gaussian and Product algorithms are examples of existing spatial modules. For nodes in the input level, the Gaussian algorithm is used and the spatial module Product is used for the top nodes of the hierarchy use.

The input vector is compared by the Gaussian algorithm without dealing with the existing matches in the match matrix. Whenever the distance between the input vector and the existing match, known as Euclidean distance, is sufficiently small, then the entry is considered as the same match, and the match count is increased and stored in memory. The distance between an input vector and previously stored vectors is

$$d^2(x, w_j) = \sum_{i=1}^{D} (x_i - w_j)^2 \quad (1)$$

where D is the dimension of the vector (64 in the first level), x_i is the *i*th element of the input vector and w_j is the position *i* of the vector *j* in the match matrix *W*. The match threshold of an input vector to an existing match is the Maximum distance parameter.

The product algorithm calculates the probability of similarity ($belief_i$) between an input in the inference and a vector that had been previously memorized by the spatial module:

$$belief_i = \prod_{j=1}^{nchildren} y_i[child_j] * x[child_j] \quad (2)$$

where *nchildren* refers to the number of secondary nodes (previous level) that the parent node has, *x* is the input vector, y_i are the vectors previously stored by the spatial module and [$child_j$] is the part of a vector obtained from *nchildren* secondary nodes.

2.3.1.2. Temporal module

The temporal module forms groups of matches in time, called temporal groups. Subsequently, a temporal match matrix is built. After the training phase, the temporal module counts on this matrix to come out the temporal groups. This module uses the sum algorithm, which takes the best representations of all groups to classify new input patterns during inference. When a new input vector is presented during the training phase, the spatial module represents the input vector as one of the learned matches.

Through the training phase, the new input vector is presented by a spatial modules as one of the learned matches. This process increases the elements (*j, i*) of the temporal match matrix and is controlled by the *transitionMemory* parameter. This increment (*It*) is calculated as follows:

It = *transitionMemory* -t +1, where t is the Training the HTM time in seconds between the current match and the past match.

2.3.2. Inference phase

After training a node, the network transitions to the inference mode. When the complete network is trained, all of the nodes are in the inference state, and the network is capable of performing inference with new input patterns. Initially, a probability distribution is generated for the categories that were used during training.

2.3.2.1. Spatial module

When an input pattern arrives to the spatial module, the network will generate a distribution of beliefs about the categories that have been created in the training phase. Both the Gaussian spatial module and the Product spatial module perform variously during the inference stage, but both come out with a belief vector from an input vector around the matches.

In the Gaussian spatial module, the distance between an input vector x and each of the trained matches w_j is calculated using equation (1).

This distance becomes a probability vector considering x as a random sample drawn from a set of multi-dimensional Gaussian probability distributions, all of them based in one of the trained matches. All of these distribution probabilities have the same constant variance in all dimensions, controlled by the *Standard Deviation* (*SD*) parameter, which is the square root of the variance. Each element i of the probability vector b, which represents the probability that the input vector x has the same cause as the match i, is calculated using the following equation:

$$y_i = \exp\left\{-\frac{d^2(x, w_j)}{2SD^2}\right\} \tag{3}$$

where d^2 is defined in equation (1) and w_j is the match of the position j in the match matrix W.

The algorithm of the Product spatial module divides the input vector at the outputs of each one of its subgroups. The algorithm uses the dot product with the same parts of the match and then calculates the products of these numbers, resulting in a probability vector element on matches in the match matrix.

2.3.2.2. Temporal module

During the inference phase, the temporal module receives a probability vector concerning the matches in the spatial module. Subsequently, the module calculates the probability distribution of the groups. A choice is made between two different algorithms in the temporal module during the inference: *maxProp* and *sumProp*, controlled by the *PoolerAlgorithm* time parameter. These algorithms are defined in detail in (George and Jaros, 2007).

2.4. HTM design and implementation

As commented before, the HTM network used for this experiment was implemented using the HTM Nupic API, developed by Numenta®. Having Python API, it is a programming framework that can be used to set up custom experiments. Despite the long-time of execution, writing a training script is made easy for researchers through the automation API. Python must be used for writing these training scripts and after each level in the network; results can be saved by researchers to minimize the effect of the runtime failure.

Configuration of the training process and handling of the information are done so the information flows in network built with defined architecture. The number of iterations performed with the training images is considered as key parameter here. In this case, 2000 iterations were performed at three levels. Experiments have demonstrated that increasing up to double the number of iterations (4000) does not result in a significant increase in the accuracy of the analysis (Perea et al., 2009, 2012a, 2012b). In Table 1, the most relevant parameters of the network-training phase are presented, as are the starting values of the core network as recommended by (Numenta Inc., 2010).

Table 1. Parameters used during training.

Parameter	Description	Values
maxDistance (maxDist)	Minimum Euclidean distance for storing a pattern as a new category, in the lower level of the training phase.	1
Scale factor (ScaleCount)	Number of scales of the same image that the sensor introduces into the network.	1
Spatial reference (spatialRF)	Size of the information reception field with respect to the total.	0.2
Temporal groups (requestGroupCount)	Temporal groups that will be created: Sets the maximum number.	24
Spatial overlap (spatialOverlap)	Overlap between nodes of the same level according to the information received from child nodes.	0.5
Scale reference (scaleRF)	Number of scales of which the node receives information.	2
Categories (outputElementCount)	Number of categories.	3

Information flows through an architecture that needs to be determined; the processing of the information and the training are only set once the network is built. Meanwhile the processing analysis is being carried out, user interface of NuPIC allows interaction with the network.

Figure 5 shows the training of temporal module of level 1, sub-level 2. The information given by the spatial node of the first spatial module is presented just next to the training image. This first level uses a filter (Gabor filter) to help in recognizing input patterns and making a selection among a series of categories based on geometric and temporal similarities. Used in image processing for purposes of texture analysis and feature extraction, Gabor filters are known as bandpass filters whose impulse response is obtained through a multiplication of Gaussian envelope functions with a complex oscillation (Weldon et al., 1996). According to Gabor, space (time) uncertainty product are shown through these elementary function. Filters, selective for orientation, are possibly created through the extension of these functions to two dimensions.

When the network is trained, the new data stream in this sub-layer will be compared to the memorized sequences performing an initial classification.

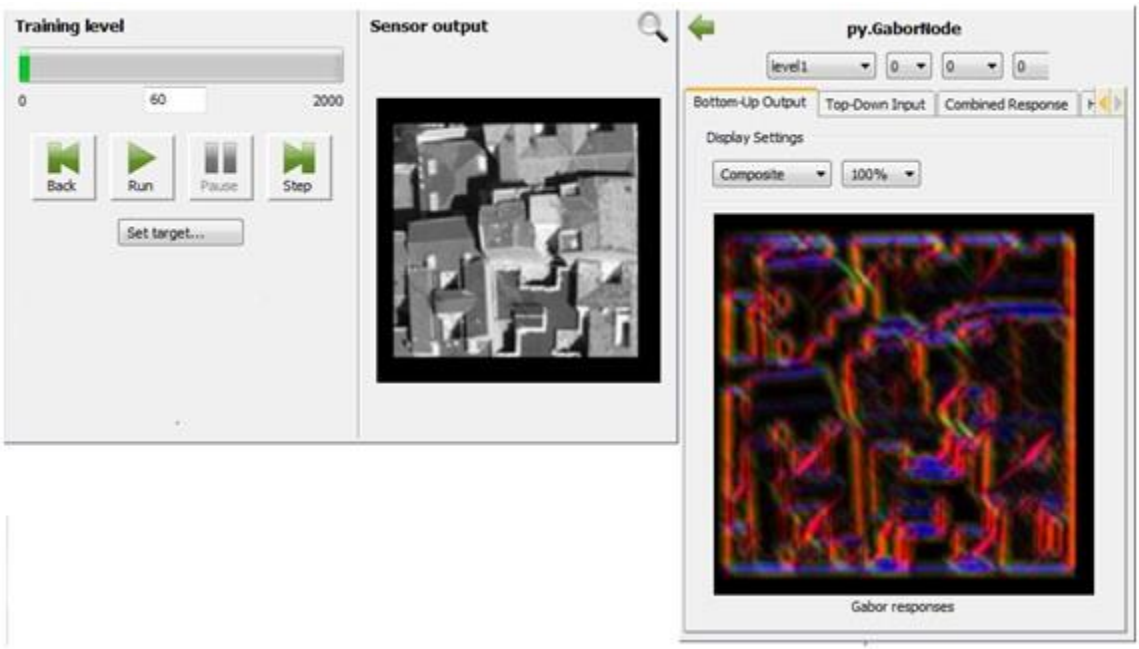

Figure 5. Training stage of level 1, sub-level 2.

2.6.3. Inference phase

The inference stage starts only after stating the categories and training the network with the provided database. According with images learned and memorized from the previous stage, the interference stage implies the network to analyse unknown images. In Figure 6, it is presented the system working on the inference stage where the first sub-level of the node creates a representation depending to the known

patterns having very close shape and texture. Once the inference stage is completed, a confusion matrix is obtained.

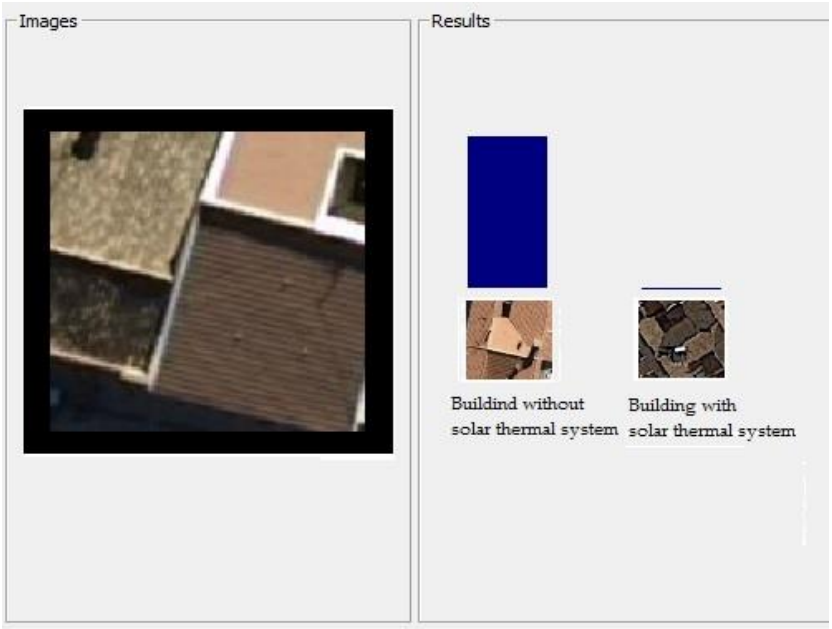

Figure 6. Example of inference stage.

3. Results and discussion

During the experiments, internal network parameters that affect the learning process were modified, with the main goal of obtaining an optimal methodology for the recognition of image patterns. To confirm the outcomes of this analysis, visual inspection results are compared with the ones obtained from the proposed method.

As mentioned above, the *maxDist* parameter defined the Euclidean distance between a familar pattern and a new one, which is analytical in the recognition and classification of patterns. An optimal value is essential for the successful creation of temporal groups during the training phase. A high value of the *maxDist* parameter contributes to the formation of fewer temporal groups, which could seriously impact the total recognition accuracy. On the other hand, a low value of the *maxDist* parameter generates a high number of temporal groups, which on top of the large memory demand also results in poor recognition performance. To avoid these undesirable effects, it is very important to evaluate the optimal value for *maxDist* to achieve the best accuracy in the classifications.

In the original configuration, the *maxDist* parameter has a starting value of 1, and the influence of this parameter on the overall accuracy values in the different classifications was studied. The *maxDist* values (Table 2) used in this experiment were defined based on the results of the initial studies performed (Perea et al., 2016, 2017).

Table 2. Percentage of overall accuracy and averages of coincidences and temporal groups of the 64 bottom nodes for various values of *maxDist*.

maxDist	Overall accuracy (%)	Number of coincidences	Number of temporal groups
1	88.94	57.00	17.00
3	96.35	46.00	12.00
6	84.17	19.00	10.00
9	78.87	13.00	3.00
12	67.39	11.00	2.00

Table 2 presents the *maxDist* parameter values with respect to the overall accuracy obtained for each of the test classifications. The maximum accuracy value was 96.89% and was obtained at an intermediate value for a *maxDist* of 3. After this value, there is nearly a linear drop in the overall accuracy of the classifications. This drop is due to the number of coincidences detected during the training phase and the temporal groups formed.

For the previously mentioned optimal value of *maxDist*, the Urban class was the class that obtained the largest number of misclassified frames, as seen in Table 3, whereas the Grape class reached the highest accuracy of all of the classes during classification.

Table 3. Solar thermal confusion matrix for the optimum value of maxDist.

Building system	Without	With
Without	969	31
With	42	958

Looking at the second and third columns of Table 2, a large number of matches was not related to a greater overall accuracy of classification, as the number of matches in input patterns might be unrealistic, classifying new similar patterns in different categories. For example, if we set a low value for the parameter *maxDist*, it is forcing the creation of many different, but similar, groups. So, several categories may correspond to the same pattern.

For the case with *maxDist* of 3, which can be considered optimal, the number of matches obtained was 46. On the other hand, the effect of the value of the *maxDist* parameter on the creation of temporal groups during the training phase of the network can be seen in Table 2; the smaller the *maxDist* parameter, the greater the number of temporal groups was obtained, leading similar patterns to be classified in different classes. Conversely, increasing the value of the *maxDist* parameter reduces the formation of temporal

groups, an effect that is not conducive in any way to obtaining an optimal accuracy in the classification, as the images of wineries and images of forest areas are classified in the same category (Table 4). For the case with the optimal *maxDist* value of 3, the number of temporal groups obtained was 12.

Table 4. Solar thermal confusion matrix for a maxDist value of 12.

Building system	Without	With
Without	772	228
With	427	573

The effect of the *SD* parameter on the accuracy of the classification was verified. This parameter is calculated as the square root of the *maxDist*. This value is a justifiable starting value for SD because the distances between the matches are calculated as the square of the Euclidean distance instead of the normalized Euclidean distance.

Figure 7 presents the overall accuracy values obtained for different *SD* values. Similar to the *maxDist* parameter, there is growth in the overall accuracy value until it reaches a maximum of 96.35% for an SD value of 1.73. Smaller *SD* parameter values cause high beliefs to be assigned only to matches that are very close to the inferred pattern. Conversely, when using lower *SD* values, between 1 and 1.73, all of the matches receive high belief values independent of their distance to the inferred pattern. Based on the optimal *maxDist* and *SD* values previously discussed, we studied the effect of the *ScaleRF* and *ScaleOverlap* parameters on the network training and overall accuracy obtained in the classification of the images.

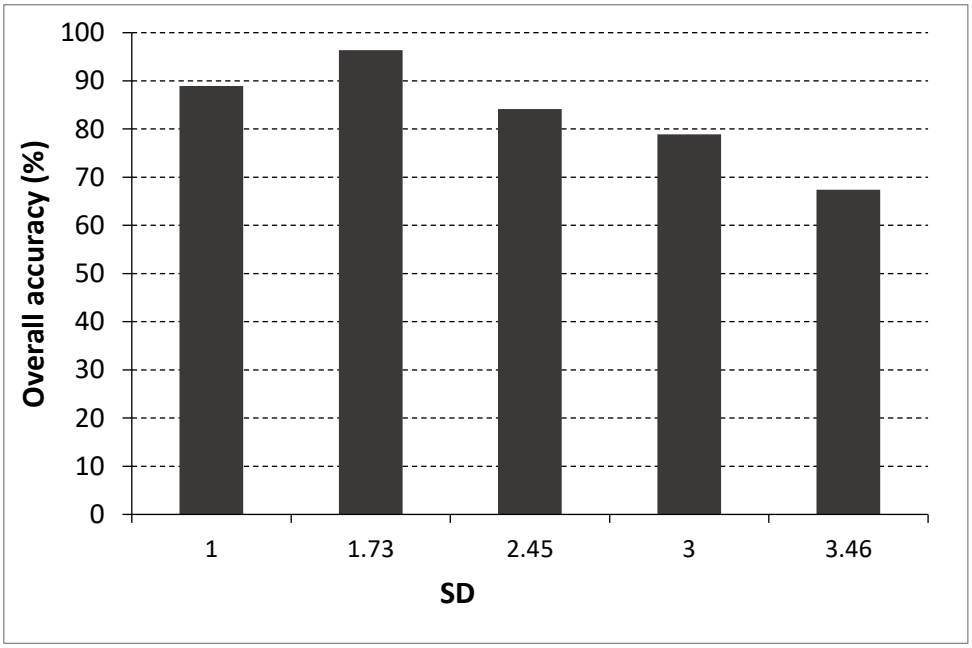

Figure 7. Overall accuracy for five setups of the *SD* parameter.

As mentioned above, the *scaleRF* and *ScaleOverlap* parameters are relevant to the scale or the resolution of the images that are conferred to the network; thus, by varying these parameters, we can change the number of distinct scales of the image that are presented to the nodes and the overlap among them.

This change is sensitive because changes in the image resolutions allow the network to extract patterns of the same image in different levels to create invariant representations (or models of stored patterns) used to classify new images. Classification of new images by consistent representations created (or models of stored patterns) is allowed by the network extracting patterns of the same image sue to variations in image resolutions which make the change very sensitive.

The elemental network starts from intermediate values of *ScaleOverlap* and *ScaleRF* (1 and 1, respectively). Figure 8 presents a bar chart in which the *ScaleOverlap* and the *ScaleRF* parameter are related to the overall accuracy for each case. The highest overall accuracy (98.05%) was obtained for a value of 4 for the *scaleRF* parameter and 1 for the *scaleOverlap*. The worst results were retrieved for a *ScaleOverlap* parameter value of 0; this value creates no spatial overlap among the input patterns, worsening the training stage in the temporal module and thereby reducing the number of temporal groups formed and their time sequence.

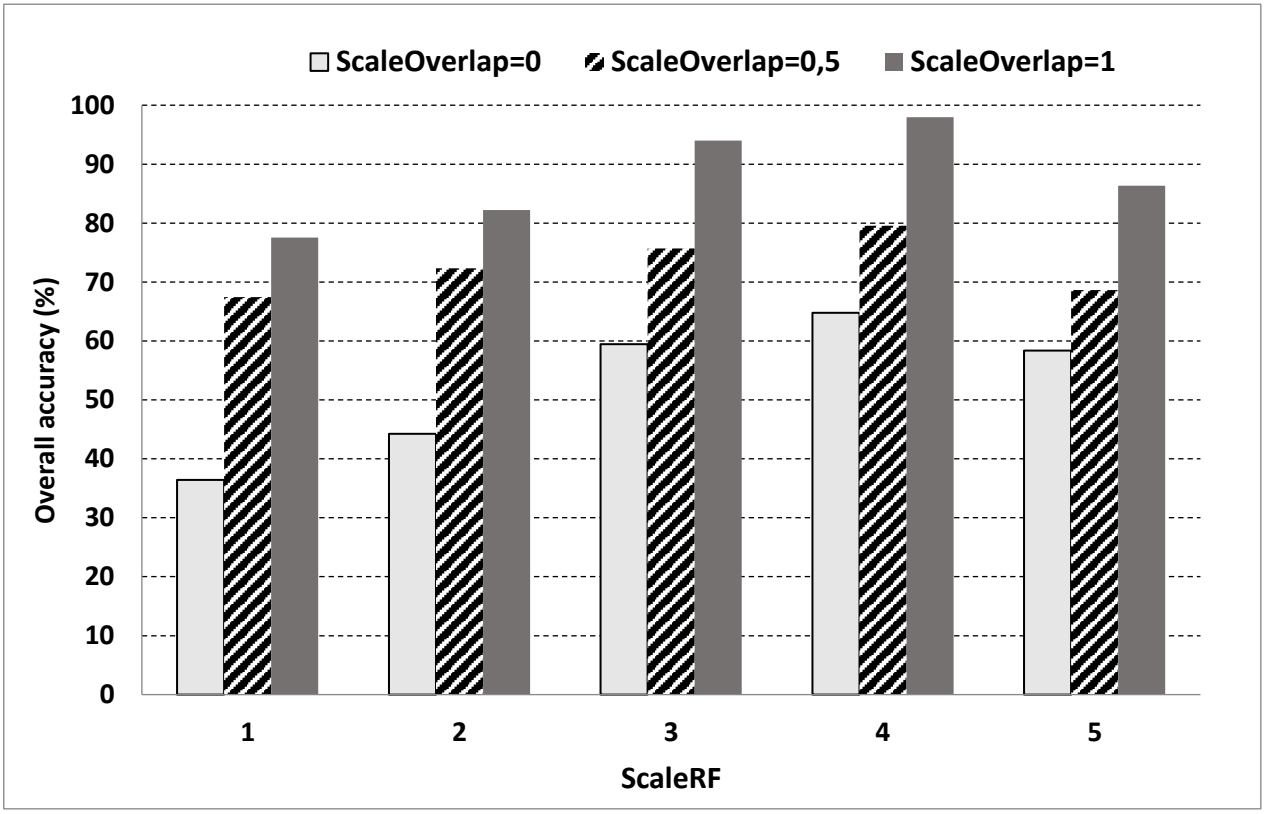

Figure 8. Values of *scaleRF* and *ScaleOverlap*.

In general, it is observed in this study that a value of 4 for the *ScaleRF* parameter optimizes the capacity of the network to extract patterns from images at different resolutions. From a value of 5, the overall classification accuracy starts to fall again.

We compared our results to those of other works. For example, Samsudin et al. (2016) used surface classifications and spectral indices in satellite multispectral remote sensing data to generate degradation status maps of concrete and metal roofing materials and obtained an overall accuracy of 94.17%;

Estimation of geographical PV potentials for buildings in downtown San Francisco is the objective of the object oriented classification method and LiDAR data employed by Li et al. (2015b); however some boundary problems were faced by the research next to data accuracy of LiDAR in terms of both building footprint extraction and 3D modelling.

In our performance, the maximum overall accuracy obtained among the different classifications made was 98.05%, avoiding problems related to the use of images with high spatial resolution, as in the salt-and-pepper noise effect. This effect makes it difficult to obtain and cleanly classify images, resulting in different cases for a plot where there should only be a single case.

In Table 5 the results of the Confusion matrix are presented. Only in 15 frames, the Building without solar thermal system class was classified as the Building with solar thermal system class, and in 24 frames, it was classified as Building without solar thermal system class. The higher accuracy obtained guarantee the success of the methodology proposed.

Therefore, the accuracy value obtained from the classification using the algorithm based on HTM is similar or superior to values obtained by other authors using object-oriented classification and neural networks, which demonstrates that the methodology is appropriate for the identification of building roofs in order to assess the opportunities available to install solar thermal systems in small urban areas.

Table 5. Solar thermal confusion matrix of the best performing system.

Building system	**Without**	**With**
Without	985	15
With	24	976

In Figure 9, 747 buildings in the study area, which represents about 92% of the total rooftops area, would be suitable for solar thermal systems.

Figure 9. Classification view.

Although there are similar works to estimate the possibility of using solar energy roofs, these are pixel-based approach (Li et al., 2015) and therefore are not as accurate as the method proposed here.

Regarding the environmental aspects, burning fossil fuels to generate the energy to heat water will result harmful in gas emissions. The potential decrement in greenhouse gases by cause of the installation of solar thermal systems on these rooftops was also estimated based on experimental results. Considering that the type of housing in the area is residential building with 4 dwellings per floor and that in each dwelling there is an average saving in electricity of 1.25 MWh (US DOE, 2007) due to the implementation of the solar thermal systems, multiplied by the 747 buildings analyzed, a total saving of 14940 MWh is obtained. As shown in Table 6, for a village of 7000 inhabitants, implementing the solar thermal systems in the case study (747 buildings without solar thermal systems) would produce decreases of 9830.52 tons of carbon dioxide (CO_2), 0.114 tons of methane (CH_4), and 0.141 tons of nitrous oxide (N_2O) emissions annually. This means a saving of 1.4 tons of CO_2 per inhabitant.

Regarding the economic aspects, the installation costs are around 600 €/m^2 collector with a maintenance costs of 10 €/m^2 collector/year (Izquierdo et al. 2011). Thus, the energy payback-time can be defined as the time necessary for a solar equipment to collect the energy (valued as primary) equivalent to that used to produce it. Solar flat collectors can last between 15 and 20 years. Ardenbte et al. (2005) show the great economical convenience of this technology because the energy payback-time resulted less than 2 years for a house with 3 persons, and this is considered very low. Of course, if the persons living in the same house are increased the pay-back time will be smaller. Nowadays it can be say that the use of the solar thermal energy is a mature and reliable technology, that the investments realized in general are amortizable without the necessity of subsidies, and that it is an alternative respectful with the environment (Juaidi et al., 2016).

In Spain, regarding the social aspects, with the Code of Technical Building (MVIV, 2009), and as specified in its Basic Document HE (Energy Saving), all new buildings are required to install solar thermal energy systems. This law has supposed a definitive impulse to this technology, because the minimum of the total hot water demand must be 70% from solar thermal systems. In recent years, there has been a notable increase in solar thermal installations due, on the one hand, to the greater social and political sensitivity towards environmental issues and, on the other hand, to the continuous improvement and reduction of costs of solar thermal systems (Montoya et al., 2014) .

Table 6. Annual environmental benefits from gases reductions.

Gas	Acronym	Electricity saving	Emissions	Total emissions reduced
		MWh	**kg/MWh**	**Tons**
Nitrous Oxide	**N_2O**	14900	0.00941	0.140
Methane	**CH_4**	14900	0.00762	0.114
Carbon Dioxide	**CO_2**	14900	658	9804.2

4. Conclusions

This work presents a novel procedure for determining roof surfaces suitable for the instalment of solar thermal systems in small urban areas. A novel technology of Hierarchical Temporal Memory Algorithm (HTM) is used to develop experimental analysis and classification of images of urban environments. After changing multiple parameters related to architecture and inner workings, analysis of sample images

are carried for several repetitions during the learning and analysis process. The maximum overall accuracy obtained among the different classifications made was 98.05%, avoiding problems related to the use of images with high spatial resolution, as in the salt-and-pepper noise effect. Lessons learned from the case of study which have applied the automatic detection of solar collector in roof tops may inform on how municipalities might energy saving. In this case of study, 9804.2 tons of carbon dioxide (CO_2), 0.114 tons of methane (CH_4), and 0.140 tons of nitrous oxide (N_2O) emissions can be decremented annually through the implementation of solar thermal systems. Assessing the feasible opportunities for solar thermals systems installation is possible by generalizing the presented tested methodology to other urban areas. As main conclusion, the assessment of rooftop potential for solar flat plate collector is an essential component of research focusing on energy saving options for the cities. This potential is essential because it is the only supply resource which all cities possess in the face of looming environmental and economic risks.

References

AlFaris, F., Juaidi, A., & Manzano-Agugliaro, F. (2016). Energy retrofit strategies for housing sector in the arid climate. *Energy and Buildings*, *131*, 158-171.

Almeida, C. M. V. B., Agostinho, F., Huisingh, D., & Giannetti, B. F. (2017). Cleaner production towards a sustainable transition. *Journal of Cleaner Production*, *142*, 1-7.

Andreopoulos, A., Tsotsos, J. K. (2013). 50 years of object recognition: Directions forward. *Computer Vision and Image Understanding*, *117*(8), 827-891.

Ardente, F., Beccali, G., Cellura, M., & Brano, V. L. (2005). Life cycle assessment of a solar thermal collector: sensitivity analysis, energy and environmental balances. Renewable Energy, 30(2), 109-130.

Baños, R., Manzano-Agugliaro, F., Montoya, F. G., Gil, C., Alcayde, A., & Gómez, J. (2011). Optimization methods applied to renewable and sustainable energy: A review. *Renewable and Sustainable Energy Reviews*, 15(4), 1753-1766.

Battiato, S., Farinella, G. M., Furnari, A., Puglisi, G., Snijders, A., & Spiekstra, J. (2015). An integrated system for vehicle tracking and classification. *Expert Systems with Applications*, *42*(21), 7263-7275.

Boone, A., Karnowski, T. P., Chaum, E., Giancardo, L., Li, Y., & Tobin, K. W. (2010, May). *Image processing and hierarchical temporal memories for automated retina analysis.* In Biomedical Sciences and Engineering Conference (BSEC), IEEE Conference on, Oak Ridge, USA, 25-26 May 2010. IEEE: San Diego, CA, USA, 2010.

Cadez, S., Czerny, A. (2016). Climate change mitigation strategies in carbon-intensive firms. *Journal of Cleaner Production, 112*, 4132-4143.

Castellano, N., Parra, J. A. G., Valls-Guirado, J., & Manzano-Agugliaro, F. (2015). Optimal displacement of photovoltaic array's rows using a novel shading model. *Applied Energy*, *144*, 1-9.

Fernández-García, A Rojas, E., Pérez, M., Silva, R., Hernández-Escobedo, Q., & Manzano-Agugliaro, F. (2015). A parabolic-trough collector for cleaner industrial process heat. *Journal of Cleaner Production*, 89, 272-285.

George, D., Jaros, B. *The HTM learning algorithms.* Numenta, Inc.: Redwood city, USA, 2007.

Hare, S. Saffari, A., & Torr, P. H. Efficient online structured output learning for keypoint-based object tracking. In *Computer Vision and Pattern Recognition (CVPR)*, IEEE Conference on, Providence, USA, 16-21 june 2012; IEEE: San Diego, CA, USA, 2012, 1894-1901.

Hawkins, J. Ahmad, S., & Dubinsky, D. Hierarchical temporal memory including HTM cortical learning algorithms. Available on: http://numenta.org/resources/HTM_CorticalLearningAlgorithms.pdf (accesed on 19 October 2015).

Hawkins, J.; & Blakeslee, S. *On Intelligence*. 1st Ed.; Henry Holt: New York, USA, 2004; pp. 296.

Hawkins, J., & George, D. *Hierarchical Temporal Memory, Concepts, Theory, and Terminology.* Inc.: Redwood city, USA, 2007.

Izquierdo, S., Montañés, C., Dopazo, C., & Fueyo, N. (2011). Roof-top solar energy potential under performance-based building energy codes: The case of Spain. Solar Energy, 85(1), 208-213.

Juaidi, A., Montoya, F. G., Ibrik, I. H., & Manzano-Agugliaro, F. (2016). An overview of renewable energy potential in Palestine. Renewable and Sustainable Energy Reviews, 65, 943-960.

Kohli, D., Sliuzas, R., & Stein, A. (2016). Urban slum detection using texture and spatial metrics derived from satellite imagery. *Journal of Spatial Science*, 1-22.

Li, Y., Ding, D., Liu, C., & Wang, C. (2016). A pixel-based approach to estimation of solar energy potential on building roofs. *Energy and Buildings*, *129*, 563-573.

Li, Y., Gong, J., Wang, D., An, L., & Li, R. (2013). Sloping farmland identification using hierarchical classification in the Xi-He region of China. *International journal of remote sensing*, *34*(2), 545-562.

Li, Y., Wang, S., Tian, Q., & Ding, X. (2015a). Feature representation for statistical-learning-based object detection: A review. *Pattern Recognition*, *48*(11), 3542-3559.

Li, Z., Zhang, Z., & Davey, K. (2015b). Estimating geographical pv potential using lidar data for buildings in downtown san francisco. *Transactions in GIS*, *19*(6), 930-963.

Manzano-Agugliaro, F., Montoya, F. G., Sabio-Ortega, A., & García-Cruz, A. (2015). Review of bioclimatic architecture strategies for achieving thermal comfort. *Renewable and Sustainable Energy Reviews*, *49*, 736-755.

Manzano-Agugliaro, F., Sanchez-Muros, M. J., Barroso, F. G., Martínez-Sánchez, A., Rojo, S., & Pérez-Bañón, C. (2012). Insects for biodiesel production. *Renewable and Sustainable Energy Reviews*, *16*(6), 3744-3753.

Martínez-Rubio, A., Sanz-Adan, F., Santamaría-Peña, J., & Martínez, A. (2016). Evaluating solar irradiance over facades in high building cities, based on LiDAR technology. *Applied Energy*, *183*, 133-147.

Mekhilef, S., Saidur, R., & Safari, A. (2011). A review on solar energy use in industries. *Renewable and Sustainable Energy Reviews*, *15*(4), 1777-1790.

Montoya, F. G., Aguilera, M. J., & Manzano-Agugliaro, F. (2014). Renewable energy production in Spain: A review. Renewable and Sustainable Energy Reviews, 33, 509-531.

MVIV, April 2009. Ministry of Housing (Spanish Government). Technical Building Code (RD 314/2006, March 17th; and RD 1371/2007, October 19th); Basic Document: Minimum Coverage of Service Hot Water and Photovoltaic Energy (DB HE4 and DB HE5) (in Spanish).

Numenta Inc. *HTM cortical Learning Algorithms.* Numenta, Inc.: Redwood city, USA, 2010.

Perea-Moreno, A. J., Aguilera-Ureña, M. J., & Manzano-Agugliaro, F. (2016). Fuel properties of avocado stone. *Fuel*, *186*, 358-364.

Perea, A. J., Ureña, M. J. A., De Larriva, J. E. M., & Agugliaro, F. M. (2017). Empleo de la Fotogrametría Digital para la Evaluación del Suelo con Riesgo de Erosión en Olivar. Dyna, 92(1), pp 55-62.

Perea-Moreno, A. J., Aguilera-Ureña, M. J., Meroño-De Larriva, J. E., & Manzano-Agugliaro, F. (2016). Assessment of the Potential of UAV Video Image Analysis for Planning Irrigation Needs of Golf Courses. Water, 8(12), 584.

Redweik, P., Catita, C., & Brito, M. (2013). Solar energy potential on roofs and facades in an urban landscape. *Solar Energy*, *97*, 332-341.

Rozado, D., Rodriguez, F. B., & Varona, P. (2012). Extending the bioinspired hierarchical temporal memory paradigm for sign language recognition. *Neurocomputing*, *79*, 75-86.

Szabó, S., Enyedi, P., Horváth, M., Kovács, Z., Burai, P., Csoknyai, T., & Szabó, G. (2016). Automated registration of potential locations for solar energy production with Light Detection And Ranging (LiDAR) and small format photogrammetry. *Journal of Cleaner Production*, 112, 3820-3829.

Samsudin, S. H., Shafri, H. Z., & Hamedianfar, A. (2016). Development of spectral indices for roofing material condition status detection using field spectroscopy and WorldView-3 data. *Journal of Applied Remote Sensing*, *10*(2), 025021-025021.

Siddiqi, M. H., Ali, R., Khan, A. M., Kim, E. S., Kim, G. J., & Lee, S. (2015). Facial expression recognition using active contour-based face detection, facial movement-based feature extraction, and non-linear feature selection. *Multimedia Systems*, *21*(6), 541-555.

Torres-Sánchez, J., López-Granados, F., & Peña, J. M. (2015). An automatic object-based method for optimal thresholding in UAV images: Application for vegetation detection in herbaceous crops. *Computers and Electronics in Agriculture*, *114*, 43-52.

US DOE (2007). Electricity emission factors. Available at, http://www.eia.doe.gov/oiaf/1605/pdf/Appendix%20F_r071023.pdf.

Weldon, T. P., Higgins, W. E., & Dunn, D. F. (1996). Efficient Gabor filter design for texture segmentation. *Pattern Recognition*, *29*(12), 2005-2015.